Xylose assimilation in heterotrophic *Auxenochlorella protothecoides*: Unlocking the potential of microalgae for xylitol bioproduction

Pablo Perez Saura[1], Pierre Cardol[1], Claire Remacle[1]*

[1]Laboratory of genetics and physiology of microalgae, InBios/Phytosystems Research Unit, University of Liège, Belgium

ORCID: Pablo Perez-Saura: 0000-0002-9823-685X; Pierre Cardol: 0000-0001-9799-0546; Claire Remacle: 0000-0002-5016-9547

***Corresponding Author:** c.remacle@uliege.be

Abstract

Xylitol is a high-value sugar alcohol widely used in the food and pharmaceutical industries. While microbial xylitol production primarily relies on fermentative organisms, sustainable alternatives involving photosynthetic microorganisms as a substitute for chemical hydrogenation remain largely unexplored. Here, we investigate whether the microalga *Auxenochlorella protothecoides* UTEX 25 can assimilate xylose and produce xylitol under heterotrophic conditions when glucose, acetate, or both carbon sources were simultaneously provided to the medium. When supplemented with glucose, xylose uptake was initially inhibited but later accelerated, leading to the highest xylose consumption rate (0.84 ± 0.10 g gDW^{-1} d^{-1}). When supplemented with acetate, xylose assimilation occurred gradually with a lower consumption rate (0.24 ± 0.01 g gDW^{-1} d^{-1}). Xylose uptake was linked to xylitol excretion, with a 1:1 xylose-to-xylitol conversion ratio in all conditions. When supplemented with both carbon sources, xylose metabolism was enhanced, combining the benefits of both glucose-induced transport and acetate-sustained metabolism. This condition resulted in an intermediate xylose consumption rate (0.64 ± 0.06 g gDW^{-1} d^{-1}) and the highest xylitol production rate (0.65 ± 0.01 g gDW^{-1} d^{-1}). A fed-batch strategy further improved xylose conversion and increased final xylitol yield to 0.91 g g_{xylose}^{-1}, comparable to xylitol bioproduction rates in engineered yeasts. Genome analysis identified putative xylose transporters and a putative xylose reductase. These findings establish *A. protothecoides* as a promising candidate for microalgal-based xylitol production, providing a foundation for further metabolic engineering and process optimization for sustainable xylose valorization.

Keywords:

Xylose reductase, acetate, glucose, carbon metabolism, sugar transporter, green alga

Authors' contributions

Pablo Perez Saura: Writing – original draft, Writing – review & editing, Conceptualization, Methodology. Claire Remacle: Conceptualization, Methodology, Writing – review & editing, Supervision, Funding acquisition. Pierre Cardol: Writing – review & editing.

Competing interests

The authors declare that the research was conducted in the absence of any commercial or financial relationships that could be construed as a potential conflict of interest.

Funding declaration

This work was supported by Fonds de la Recherche Scientifique (FNRS) (CDR J.0175.20 and J.0149.23 to CR and J.0025.24 to PC) ; Fonds Wetenschappelijk Onderzoek – Vlaanderen (FWO) and FNRS under the Excellence of Science (EOS) Project No. 30829584; Action de Recherche Concertée from the University of Liege (DARKMET ARC grant 17/21- 08), and ADV_BIO grant (SPF Économie, P.M.E., Classes moyennes et Énergie, Direction générale de l'Énergie).

Acknowledgements

PC is research director of Belgian Fonds de la Recherche Scientifique-FNRS. We thank M. Radoux for expert technical assistance.

Data availability

Data will be made available on request.

Declaration of Generative AI and AI-assisted technologies in the writing process

During the preparation of this work the author(s) used ChatGPT (OpenAI) for its assistance in linguistic and grammatical improvement of the manuscript. After using this tool, the authors reviewed and edited the content as needed and take full responsibility for the content of the publication.

1. Introduction

Microalgae are photosynthetic organisms, with some species also capable of efficient heterotrophic growth. Heterotrophy offers several advantages, including reduced contamination risks and the elimination of costly enclosed photobioreactors (Carone et al. 2019). Additionally, heterotrophic cultivation enhances biomass accumulation and the production of valuable biocompounds, such as lipids (Ghidossi et al. 2017). One of the main challenges in heterotrophic cultivation is selecting economically and ecologically viable carbon sources.

Hemicellulose, a major compound of lignocellulosic biomass alongside cellulose and lignin, is among the most abundant biomolecules on Earth. However, its industrial utilization is hindered by its complex structure and limited accessibility (Rao et al. 2023). Moreover, hemicellulose primarily contains xylose (18–30% of lignocellulose hydrolysate sugars), a sugar rarely assimilated by microorganisms, except for certain yeasts (reviewed in Zha et al. 2021), filamentous fungi (Sampaio et al. 2003), bacteria (Zhao et al. 2020) , and a few microalgae (Leite et al. 2015; Portillo et al. 2022).

A previous study conducted in our laboratory demonstrated that the oleaginous green microalga *Auxenochlorella protothecoides* UTEX 25 is capable of heterotrophic growth using glucose, xylose, and acetate (Perez Saura et al. 2024) the three major carbon sources found in beech wood dilute-acid hemicellulose hydrolysates (Miazek et al. 2017). *A. protothecoides* is a microalga of choice for biotechnological applications and is one of the 'food grade' microalgal strains with a GRAS (generally recognized as safe) status. It has been commercially produced for more than 50 years, for example found in pills or energetic powders because of its high protein and lipid content. In addition, this latter feature makes this microalga also attractive in the field of biofuel production (reviewed in Caporgno et al. 2019). Finally, the microalga is amenable to genetic transformation by homologous recombination (Goold et al. 2024), which paves the way to metabolic engineering and synthetic biology.

Considering the three carbon sources assimilated by *A. protothecoides*, the metabolization of glucose and acetate follows well-known pathways. Glucose is metabolized through glycolysis, whereas acetate is converted into acetyl-CoA and enters the glyoxylate cycle, a shunt of the Krebs cycle, which enables the synthesis of building blocks, such as amino acids and sugars, via gluconeogenesis (reviewed in Zhang and Fernie 2023). In contrast, xylose assimilation is less common. In yeasts, xylose can be taken up by specific xylose transporters or, if absent, through nonspecific hexose transporters. It is reduced to xylitol by a xylose reductase and xylitol is then converted to xylulose by a xylitol dehydrogenase. Xylulose is finally phosphorylated into xylulose-5-P by a xylulose kinase. Xylulose-5-P is redirected to the pentose phosphate pathway and glycolysis to sustain growth. In some bacteria, a xylose isomerase catalyzes the conversion of xylitol into xylulose, which bypasses the xylitol intermediate (reviewed in

Zhao et al. 2020). Considering *A. protothecoides*, xylose alone could not be assimilated but a decrease of the xylose concentration was measured in the cultivation medium when a mix of acetate, glucose and xylose was used for growth. It remained unclear if xylose assimilation required glucose, acetate or both carbon sources. In addition, the metabolic fate of xylose inside the cell was not determined (Perez Saura et al. 2024).

In this study, we evaluated the ability of *A. protothecoides* to utilize xylose in the presence of glucose and/or acetate and assessed the influence of these carbon sources on xylose metabolism. Additionally, we proposed a strategy to improve xylose valorization. Interestingly, we discovered that xylose uptake was associated with xylitol excretion, suggesting a partially active xylose metabolism pathway. This pathway likely involves sugar membrane transporters for xylose uptake and xylose reductase (XR) for catalyzing the reduction of xylose into xylitol.

This finding brings another biotechnological value to *A. protothecoides*. Indeed, xylitol, a widely used sucrose substitute in the agri-food and cosmetic industries, offers high sweetening power comparable to glucose but with only half of the caloric value (Umai et al. 2022). Although industrial xylitol production typically relies on the acidic hydrolysis of xylans from hemicellulose-rich materials and chemical reduction using Raney nickel (Umai et al. 2022), microbial-based xylitol production presents a more sustainable alternative, often relying on engineered bacteria and yeasts (Umai et al. 2022). Reports of xylitol excretion by wild-type microalgae remain scarce, with, to our knowledge, only one example described in the green microalga *Chlorella sorokiniana* (Zheng et al. 2014).

2. Materials and methods

a. Microalgal strain, cultivation medium, and preculture

The study was conducted on *A. protothecoides* strain SAG 211-7a (UTEX 25), obtained from the Culture Collection of Algae at Göttingen University, Germany (SAG). The cells were maintained on 1.5% agar plates with Tris-Minimal-Phosphate (TMP) medium (Gorman and Levine 1965) at 25°C under constant illumination (40 $\mu mol_{photon}\ m^{-2}\ s^{-1}$). To acclimate the cells to heterotrophic conditions prior to experimentation, they were maintained in the dark in 25 mL of liquid TMP (100 mL flask) at 27°C under constant shaking in an incubator (GroBanks®, CLF Plant Climatics, Germany or Memmert GmbH, Germany). The medium was supplemented with an equimolar carbon concentration of D-glucose, D-xylose (hereafter referred as glucose and xylose), and acetate, resulting in a final carbon atom concentration of 150 mM (mMC) (50-50-50 mMC, or 8.33 mM of glucose, 10 mM of xylose, 25 mM of sodium acetate). One liter of TMP medium contains: 2.42g Tris buffer, 400 mg NH_4Cl, 50 mg $CaCl_2{\cdot}2H_2O$, 100 mg $MgSO_4{\cdot}7H_2O$, 93.5 mg K_2HPO_4, 63.0 mg KH_2PO_4, 50 mg Na_2-EDTA$\cdot 2H_2O$, 22 mg $ZnSO_4{\cdot}7H_2O$, 11.4 mg H_3BO_3, 5.1 mg $MnCl_2{\cdot}4H_2O$, 4.9 mg $FeSO_4{\cdot}7H_2O$, 1.6 mg $CoCl_2{\cdot}6H_2O$, 1.6 mg $CuSO_4{\cdot}5H_2O$ and 1.1 mg $(NH_4)_6Mo_7O_{24}{\cdot}4H_2O$. pH was adjusted to 7.5 with HCl and the medium was sterilized in an autoclave for 20 min at 121°C. For solid TMP medium, 15 g of agar. L^{-1} were added to the solution before sterilization. After sterilization, the medium was supplemented with 0.22 µM filtered thiamine (vitamin B1) at a final concentration of 10 µM. Two sequential precultures, each lasting one week, were performed before starting the experiments in the different media described above.

b. Growth conditions and growing parameters determination

Table 1: Carbon sources supplied in each cultivation condition (GX, AX, AGX, or 2x-AGX). Values are presented as the percentage (%) or the concentration of the total amount of carbon atoms represented by the substrate (mMC), or by the equivalent molar concentration considering the specific carbon source molarity (mM). A (+) symbol in 2x-AGX specifies the substrate concentration added during the cultivation process as a fed-batch strategy.

Conditions	**Acetate**			**D-glucose**			**D-xylose**		
	%	[ ] (mM)	[ ] (mMC)	%	[ ] (mM)	[ ] (mMC)	%	[ ] (mM)	[ ] (mMC)
GX	0	0	0	66	16.67	100	33	10	50
AX	66	50	100	0	0	0	33	10	50
AGX	33	25	50	33	8.33	50	33	10	50
2x-AGX	40	25+25	50+50	40	8.33+8.33	50+50	20	10	50

Four different culture conditions were tested (**Table 1**). All cultures were inoculated with the preculture at an initial optical density at 800 nm (OD_{800}) of 0.2. Cultures were maintained in the dark at 27°C using 100 mL shaking flasks containing 25 mL of minimal medium at pH 7.5. Each condition contained 50 mMC of xylose (10 mM) supplemented with either 100 mMC of glucose (GX condition), 100 mMC of acetate (AX condition), or both at equimolar concentrations (50-50 mMC) in the AGX condition. A fed-batch 2x-AGX

condition was also tested, in which exponentially growing preculture cells were inoculated in the AGX condition. When acetate and glucose were depleted (after two days), an additional 50 mMC of acetate and 50 mMC of glucose were supplied.

The TMP medium was used as the basal liquid culture medium, with pH adjustment depending on the carbon source. For AX and AGX conditions, the initial pH was set to 7.5. In GX conditions, the 20 mM Tris-HCl buffer (pKa=8.1 at 25°C) was replaced with an equivalent amount of MES buffer (pKa=6.2 at 20°C) and the initial pH was set to 7.0. The use of MES buffer, with a lower pKa, counteracts the rapid acidification occurring when glucose and ammonium serve as sole carbon and nitrogen sources. In case of AGX, the basification of the medium by acetate uptake compensates the acidification by glucose assimilation (Perez Saura et al. 2024).

Microalgal growth was monitored spectrophotometrically cultures at 800 nm (Perkin-Elmer lambdaTM 265 UV/VIS, USA) using plastic cuvettes with a 1 cm optical path. When necessary, samples were diluted to maintain OD_{800} values between 0.1 and 0.3. The dry biomass concentration (DW) was estimated with the following equation (Perez Saura et al. 2024):

$$DW\ (g\ L^{-1}) = OD_{800}\ \times\ 0.207$$

The specific growth rate (μ), expressed in day^{-1}, was calculated during exponential phase as the slope of the OD_{800} natural log linear regression over time:

$$\mu = \frac{\ln OD_{800_2}\ -\ \ln OD_{800_1}}{t_2\ -\ t_1}$$

Biomass yield ($Y_{x/s}$) on substrate, expressed in gDW $g_{substrate}^{-1}$, was calculated as:

$$Y_{x/s} = \frac{X_{max}\ -\ X_0}{S_0\ -\ S_1}$$

Where X_0, X_{max} represent the initial and maximal DW concentration (g L^{-1}) at the start of the culture, and S_0/S_1 are the initial and final concentrations of acetate and/or glucose (g L^{-1}).

The xylose consumption and xylitol production rates, expressed in g gDW^{-1} day^{-1} were calculated as follows:

$$Xylose\ consumption\ rate = \frac{[xylose]_1 - [xylose]_2}{(t_2\ -\ t_1) \times\ \bar{X}}$$

$$Xylitol\ production\ rate = \frac{[xylitol]_2 - [xylitol]_1}{(t_2\ -\ t_1) \times\ \bar{X}}$$

Where $[xylose]_2/[xylose]_1$ and $[xylitol]_2/[xylitol]_1$ represent the highest and the lowest values of xylose or xylitol (g L^{-1}) at the time points t_2 and t_1 (in days) and $\bar{X}$ represents the average DW concentration (g L^{-1}) over the same period.

To assess statistical significance, a Fisher test was first performed to evaluate the variance homogeneity (p value < 0.05). A Student's t-test was applied to compare the two groups. If the p value was greater than 0.01, the statistical result was explicitly stated in the text.

c. Carbon source concentration determination

At the same time points as OD_{800} measurement, 1-2 mL of culture were sampled and centrifuged (16,000 x g; 3min). The supernatant was stored at -20°C for further analysis. Glucose, xylose, xylitol and acetate were quantified in 0.22 µm filtered culture supernatant by High Performance Liquid Chromatography (HPLC, Shimadzu, Japan) as described in (Perez Saura et al. 2024). Concentrations were determined by comparing chromatogram peak areas to standard calibration curves of known glucose, xylose, xylitol, or acetate concentration. The injection volume was 40 µL for all samples.

d. Protein alignments

Putative xylose transporters and xylose reductases from *A. protothecoides* UTEX 25 were identified using *Candida intermedia* glucose/xylose facilitator 1 (Q2MDH1, Ci|gxf1) (Leandro et al. 2006), and *Debaryomyces nepalensis* xylose reductase (A0A0M4HL56, Dn|akr2) (Paidimuddala et al. 2018) as queries for Tblastn searches in the PhycoCosm database (https://phycocosm.jgi.doe.gov/phycocosm/home) (Grigoriev et al. 2021). Globally protein sequence alignments were performed using Clustal Omega (Madeira et al. 2024). Experimentally determined protein structures were obtained from the Uniprot database or the RCSB Protein Data Bank. 3D structure predictions were generated using AlphaFold 3 (Abramson et al. 2024), and visualization of protein alignment was created using the ESPript 3.0 software (Robert and Gouet 2014). 3D structure representations were generated using the PyMOL™ software (v3.1.1, Schrödinger, Inc., NY, USA).

3. Results

a. Algal growth and carbon consumption

To determine whether glucose or acetate enables xylose assimilation, we first assessed the growth of *A. protothecoides* in a medium containing either glucose and xylose (GX), or acetate and xylose (AX). A medium containing both glucose and acetate along with xylose (AGX) was used as a control, based on our previous studies showing that xylose assimilation occurs under this condition (Perez Saura et al. 2024). Loss of pigmentation was found in all the cultures, as previously observed in heterotrophic conditions (Perez Saura et al. 2024) (**Suppl. Fig. S1)**. **Figure 1a** displays the cell density of the three conditions over 8 days of dark cultivation. The GX condition reached a maximal biomass

at 1.77 ± 0.08 gDW L^{-1} after 2 days, with a specific growth rate (μ) of 2.65 ± 0.02 d^{-1}, before entering the stationary phase. In contrast in the AX condition, the maximum biomass was significantly lower (0.82 ± 0.06 gDW L^{-1}), achieved after 4 days, with a growth rate that was more than twice as low (0.98 ± 0.02 d^{-1}) as in the GX condition. The AGX condition exhibited intermediate growth dynamics, reaching the stationary phase after 2 days, with a growth rate of 2.32 ± 0.06 d^{-1} and a maximum biomass of 1.13 ± 0.05 gDW L^{-1}.

As shown in **Figure 1b-c**, the stationary phase coincided with acetate or glucose depletion in GX and AX. However, in AGX (**Fig. 1d**), exponential growth phase ceased after glucose depletion, despite the presence of acetate in the medium. Complete acetate consumption followed the next day, after the culture had already entered the stationary phase. Biomass yields on substrates, calculated as biomass produced per gram of acetate and/or glucose consumed, were 0.28 ± 0.01 and 0.59 ± 0.02 gDW g^{-1} in the AX and GX conditions, respectively, with an intermediate value of 0.40 ± 0.02 gDW g^{-1} in AGX. These trends align with previous findings on *A. protothecoides* growth (Shi et al. 1999; Heredia-Arroyo et al. 2010; Perez Saura et al. 2024).

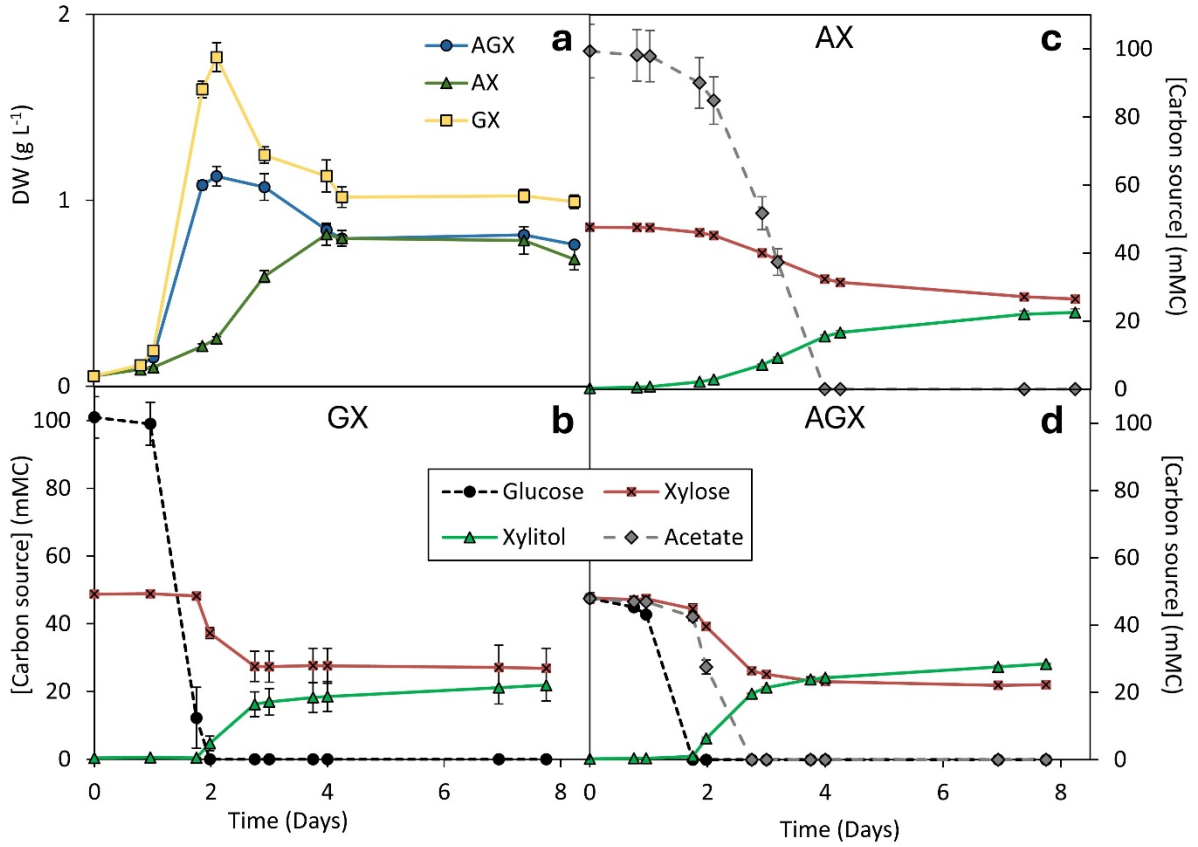

Figure 1 : Growth curves (a), and concentrations of carbon sources (b-d) in the culture medium of A. protothecoides cells grown in heterotrophy in the presence of xylose, glucose and/or acetate. Graph (a) shows dry weight evolution (in g L^{-1}) in the AGX (blue circles), AX (green triangles), and GX (yellow squares) conditions over time (days). Graphs (b-d) represent the evolution of glucose (dashed lines – black circles), acetate (dashed lines – grey diamonds), xylose (solid lines – black crossed-red squares), and xylitol (solid lines - green triangles) concentrations (expressed in mM of carbon atoms), over time (days), in the GX (b), AX (c), and AGX (d) conditions. Each value on the graphs is presented as the mean of three independent biological replicates. Error bars represent standard deviation of the mean (± SD).

Beyond the glucose and acetate consumption, all three conditions showed significant xylose uptake (**Fig. 1b-d**), demonstrating that both glucose and acetate can stimulate the process. Xylose consumption was delayed in the presence of glucose and only began after glucose depletion in both AGX and GX (**Fig. 1b**, **1d**), whereas in AX, xylose uptake occurred while acetate was still available (**Fig. 1c**). This suggests that, unlike acetate, glucose initially inhibits xylose uptake, likely due to competition for hexose or pentose transporters binding sites, as previously observed (Sun et al. 2012; Gupta et al. 2022; Badary et al. 2024). In addition, glucose is known to negatively regulate global xylose metabolism, including the xylose reductase (XR) enzymatic expression or activity (Ribeiro et al. 2021; Gupta et al. 2022). Interestingly, the presence of glucose at the start of the culture had *in fine* a positive impact on xylose consumption rate since it was about 3 times

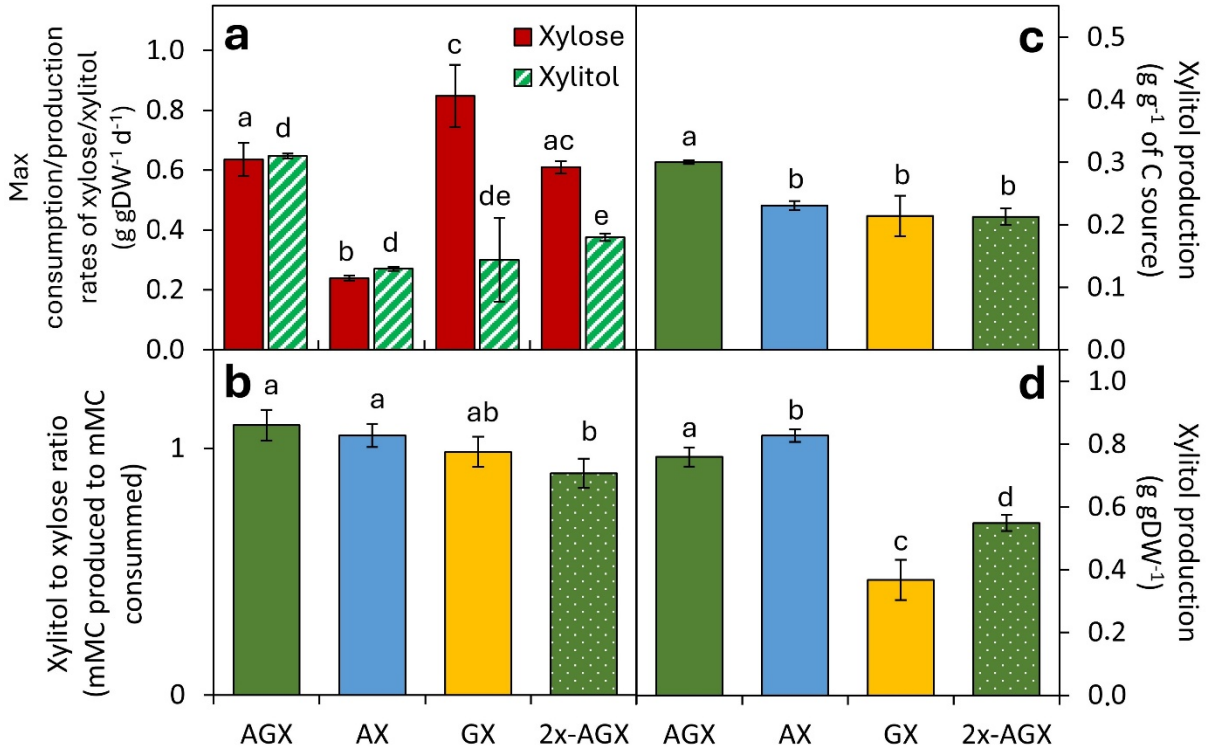

Figure 2 : Xylose and/or xylitol consumption and production parameters calculated from A. protothecoides cells grown in heterotrophy in the presence of xylose and: glucose (GX, yellow bars), acetate (AX, blue bars), or both carbon sources in batch (AGX, green bars) or fed-batch (2x-AGX, white dotted green bars) cultivation strategies. Bar-chart (a) shows the maximal xylose consumption (red solid bars) and xylitol production (green hatched bars) rates, expressed in g gDW^{-1} d^{-1}. Bar-chart (b) represents the ratio of xylitol concentration at the end of the culture compared to the xylose concentration at the beginning of the culture, expressed in mM of carbon atoms. Bar-charts (c) and (d) display the global xylitol production by the end of the culture compared to the total carbon sources consumed (acetate and/or glucose) provided at the start of the culture (c, expressed in g g^{-1}), or to the maximal achieved biomass in the condition (d, expressed in g gDW^{-1}). Each value on the graphs is presented as the mean of three independent biological replicates. Error bars represent standard deviation of the mean (± SD). Distinct letters on top of the bars indicate significantly different values within the same data group, according to a Student's t-test ($p < 0.05$).

higher in AGX (0.636 ± 0.055 g day^{-1} gDW^{-1}, *p* value < 0.01) and 4 times higher in GX (0.848 ± 0.104 g day^{-1} gDW^{-1}, *p* value < 0.01), compared to AX (0.239 ± 0.008 g day^{-1} gDW^{-1}) (**Fig. 2a**). These findings suggest that xylose uptake may be facilitated by transporters that are present in low amounts within the cell membrane (occurring in AX), with an increased

expression under glucose-induced conditions. However, these transporters do not transport xylose as long as glucose is present. A similar observation was previously reported in *C. sorokiniana* (Zheng et al., 2014), where xylose uptake was detected only after acclimation in the presence of glucose and was therefore likely mediated by nonspecific hexose transporters with some affinity for pentoses.

b. Xylose uptake is correlated to xylitol excretion

In all tested conditions, xylose consumption was accompanied by the appearance of an additional peak in high performance liquid chromatography (HPLC) analysis. By passing standards of xylose secondary metabolites through the column, we identified this peak as xylitol (**Suppl. Fig. S2**) (**Fig. 1b-d**). Unlike *C. sorokiniana*, where about 60% of the consumed xylose was converted into secreted xylitol (Zheng et al. 2014), a near 1:1 ratio xylitol-to-xylose was observed in the three conditions (AX, GX, and AGX) (**Fig. 2b)**. This suggests that while *A. protothecoides* possesses an active xylose reductase (XR) enzyme, the reduced xylitol is not further metabolized for biomass production.

Since xylitol production depended on the presence of the other carbon sources, we calculated the xylitol yield per gram of initially supplied acetate and glucose (**Fig. 2c**). No significant difference in xylitol production yield was observed between AX and GX (0.231 ± 0.007 and 0.214 ± 0.032 $g_{xylitol}\ g_{substrate}^{-1}$, respectively). However, in AGX, the yield was significantly higher at 0.300 ± 0.003 $g_{xylitol}\ g_{substrate}^{-1}$ ($p < 0.01$ vs AX, $p = 0.043$ vs GX) (**Fig. 2c**). Similarly, xylitol production rates per biomass unit followed the same trend: AGX exhibited a nearly 2 fold higher rate (0.647 ± 0.007 $g_{xylitol}\ gDW^{-1}\ d^{-1}$) compared to AX ($p$ value < 0.01) and GX (p value = 0.049) (0.270 ± 0.007, and 0.300 ± 0.140 $g_{xylitol}\ gDW^{-1}\ d^{-1}$, respectively) (**Fig. 2a**). Finally, the final xylitol concentration relative to maximal cell density is more than 2 fold lower in GX (0.367 ± 0.064 g gDW^{-1}) compared to AX and AGX (0.827 ± 0.020 g gDW^{-1} and 0.759 ± 0.031 g gDW^{-1}, respectively) (**Fig. 2d**). These results suggest that glucose facilitates high initial growth and a rapid shift to xylitol conversion but may limit the total xylitol yield due to early stationary phase onset.

c. Fed-batch cultivation enhances xylitol excretion

To improve xylose-to-xylitol conversion yield, that was around 50% (0.5 gram of xylitol per gram of xylitol) by the end of the culture in the above conditions (**Fig. 1b-d**), we implemented a fed-batch strategy under 2x-AGX condition. After two days, when glucose and acetate were depleted and xylose-to-xylitol conversion had begun, an additional supply of both carbon sources was added (**Fig. 3a**).

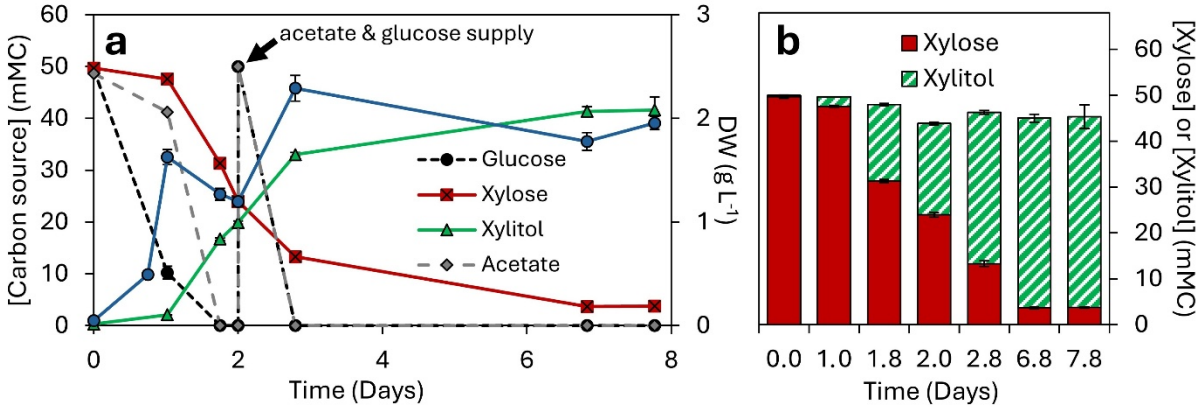

Figure 3 : Growth curves (a), and concentrations of carbon sources (a-b) in the culture medium of A. protothecoides cells grown in heterotrophy in the presence of xylose, glucose and acetate in the 2x-AGX condition. Graph (a) shows dry weight evolution (in g L^{-1}) in the 2x-AGX (blue circles) and glucose (dashed lines – black circles), acetate (dashed lines – grey diamonds), xylose (solid lines – black crossed-red squares), and xylitol (solid lines - green triangles) concentrations (expressed in mM of carbon atoms) over time (days). Bar-chart (b) shows the evolution of xylose consumption (red filled-bars) and xylitol production (green hatched-bars) over time (days). Each value on the graphs is presented as the mean of three independent biological replicates. Error bars represent standard deviation of the mean (± SD).

Following the replenishment, biomass production resumed, and acetate/glucose were rapidly consumed. Notably, the xylitol production rate remained stable until about 70% of the xylose was consumed, confirming the importance of a metabolizable carbon source in sustaining XR activity (**Fig. 3a**).

Beyond this point, biomass production, xylose consumption, and xylitol excretion gradually declined until stabilization on day 7 (**Fig. 3a**). By the end of cultivation, the xylose conversion yield was significantly improved to 90%, with only 3.7 mMC xylose remaining from an initial 49.5 mMC supplied (**Fig. 2B** & **Fig. 3a-b**). The final xylitol yield was 0.91 ± 0.06 g g_{xylose}^{-1}, comparable to the highest yields reported for wild-type yeasts such as *Candida tropicalis* JA2 (0.86 g g_{xylose}^{-1}) and *Yarrowia lipolytica* (0.97 g g_{xylose}^{-1})(Morais Junior et al. 2019; Prabhu et al. 2020), but also for engineered *E. coli* strains (~0.95 g g_{xylose}^{-1}) (Yuan et al. 2019; Umai et al. 2022).

Compared to the other conditions, the xylitol-to-xylose ratio in 2x-AGX was slightly below 1 (**Fig. 2b**), suggesting that a portion of the xylose may have been assimilated rather than excreted. Additionally, while the xylose consumption rate did not significantly differ between AGX and 2x-AGX, the xylitol production rate was markedly lower ($p < 0.01$) in 2x-AGX (0.375 ± 0.012 g gDW^{-1} d^{-1}) compared to AGX (0.647 ± 0.007 g gDW^{-1} d^{-1}) (**Fig. 2a**). Similarly, xylitol production per unit of final biomass or per gram of consumed carbon (acetate and glucose) was slightly reduced in 2x-AGX (0.548 ± 0.026 g gDW^{-1} and 0.213 ± 0.014 g $g_{substrate}^{-1}$) compared to AGX condition (0.759 ± 0.031 g gDW^{-1} and 0.300 ± 0.003 g $g_{substrate}^{-1}$) (**Fig. 2c-d**).

d. Genome analysis of *A. protothecoides*

Following the physiological characterization, we explored the genome of *A. protothecoides* UTEX 25 to identify candidate genes encoding xylose transporters and

xylose reductase (XR), using sequence homology analyses at the PhycoCosm website (Grigoriev et al. 2021).

Xylose transporters

Sugar transport in cells is mediated by membrane transporters, with xylose uptake primarily facilitated by proteins belonging to the Major Facilitator Superfamily (MFS). MFS transporters are folded into 12 transmembrane segments, with the N- and C-terminal helices facing the intracellular side. These transporters can function as facilitators, antiporters, or symporters (Drew et al. 2021). Xylose is commonly transported through proton-coupled MFS transporters (Leandro et al. 2006; Bueno et al. 2020; Drew et al. 2021). One example is the glucose/xylose facilitator 1 of *Candida intermedia* PYCC 4715 (Ci|gxf1) (Leandro et al. 2006; Fonseca et al. 2011), which is the most efficient xylose transporter when expressed in *Saccharomyces cerevisiae* (Runquist et al. 2010).

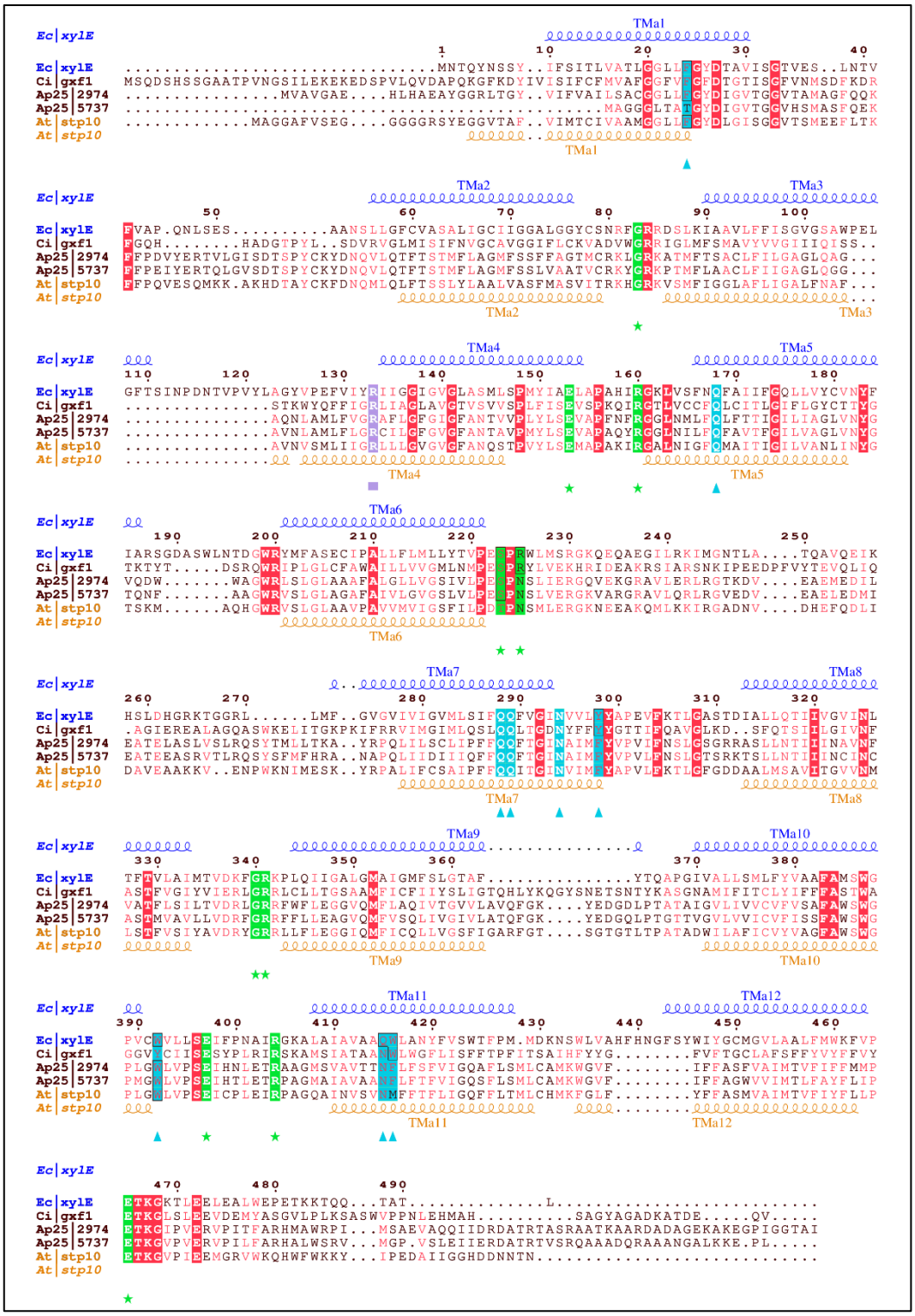

Figure 4 : Global alignment of xylose transporters of E. coli (Ec|xylE), C. intermedia (Ci|gfx1), and A. thaliana (At|stp10) with two putative A. protothecoides xylose transporters (Ap|2974 and Ap|5737). Boxes with white characters in bold show amino acid residues with strict identity. Red characters show conserved function in amino acid residues among groups. Blue triangle labels show positions of key amino acid residues for xylose coordination. Green star labels show positions of key amino acid residues for sugar transporter (SP) signature. Black frames highlight strictly conserved amino acid residues across groups compared to Ec|XylE. Top secondary structures (in blue) show predicted transmembrane alpha helices in Ec|xylE. Bottom secondary structures (in orange) show predicted transmembrane alpha helices in At|stp10.

1

A bioinformatic search using Ci|gxf1 as a query identified two putative xylose transporters in *A. prototheco*ides, designated Ap|2974 and Ap|5737, with 25.93% and 27.08% sequence identity to Ci|gxf1, respectively. These proteins also showed 25.55% and 27.31 identity to Ec|xylE, a high-affinity D-xylose:H^+ symporter from *E. coli* (Sun et al. 2012), and 47.84% and 48.13% identity to STP10 from *A. thaliana* (At|stp10), a well-characterized hexose:H^+ symporter (Paulsen et al. 2019; Bueno et al. 2020). Both Ap|2974 and Ap|5737 retained the characteristic 12 transmembrane domains and four internal helices typical of MFS sugar transporters, as shown in **Suppl. Fig. S3**. However, Ap|5737 is truncated by 16 amino acid residues at the N-terminal region compared to the crystal structures of Ec|xylE (Sun et al. 2012) and At|stp10 (Paulsen et al. 2019), leading to an incomplete first transmembrane domain, which reduces the probabilities for a putative activity.

The sugar transporter (SP) signature, responsible for coupling sugar transport with proton movement, was well preserved in both *A. prototheco*ides transporters (**Fig. 4**, **Table S1**). A notable exception was at position 225 of Ec|xylE (Sun et al. 2012) where an Arginine was found in Ci|gxf1 but replaced by an Asparagine in Ap|2974 and Ap|5737. Since At|stp10, a functional sugar/H+ symporter, also contains a Asn residue at this position (Paulsen et al. 2019), this substitution is unlikely to impair function of Ap|2974 and Ap|5737.

Amino acids implicated in xylose binding and coordination are predominantly located at the C-terminal end of the transporter and include polar residues with hydroxyl groups, facilitating hydrogen bonding, and aromatic residues that create a hydrophobic cavity to retain xylose (Faham et al. 2008; Sun et al. 2012). On the nine functionally-validated xylose-coordinating residues in Ec|xylE (Sun et al. 2012), six were conserved in Ap|2974 (**Fig. 4, Table S1**). The observed substitutions Q415N, Y298F, and W416F are unlikely to impact function, as Q415N is also present in Ci|gxf1, an efficient xylose transporter (Runquist et al. 2010), and the two aromatic substitutions unlikely impact xylose coordination (Faham et al. 2008; Sun et al. 2012). Conversely, Ap|5737 displayed an additional substitution: F24T (Ec|xylE numbering). Previous studies showed that an F24A mutation in Ec|XylE impaired transport due to a loss of substrate stabilization (Bueno et al. 2020). Given this and the truncated transmembrane domain, Ap|5737 is unlikely to be functional as a xylose transporter.

Overall, Ap|2974 appears to be the most promising candidate for xylose transport in *A. prototheco*ides. However, further experimental validation is required to assess its specificity and functionality.

Xylose reductase

To identify a putative xylose reductase (XR) in *A. prototheco*ides UTEX 25 genome, we conducted a bioinformatic search using a well-characterized XR from *Debaryomyces nepalensis* (Dn|akr2), a member of aldose-keto reductase (AKR) NAD(P)H-dependent

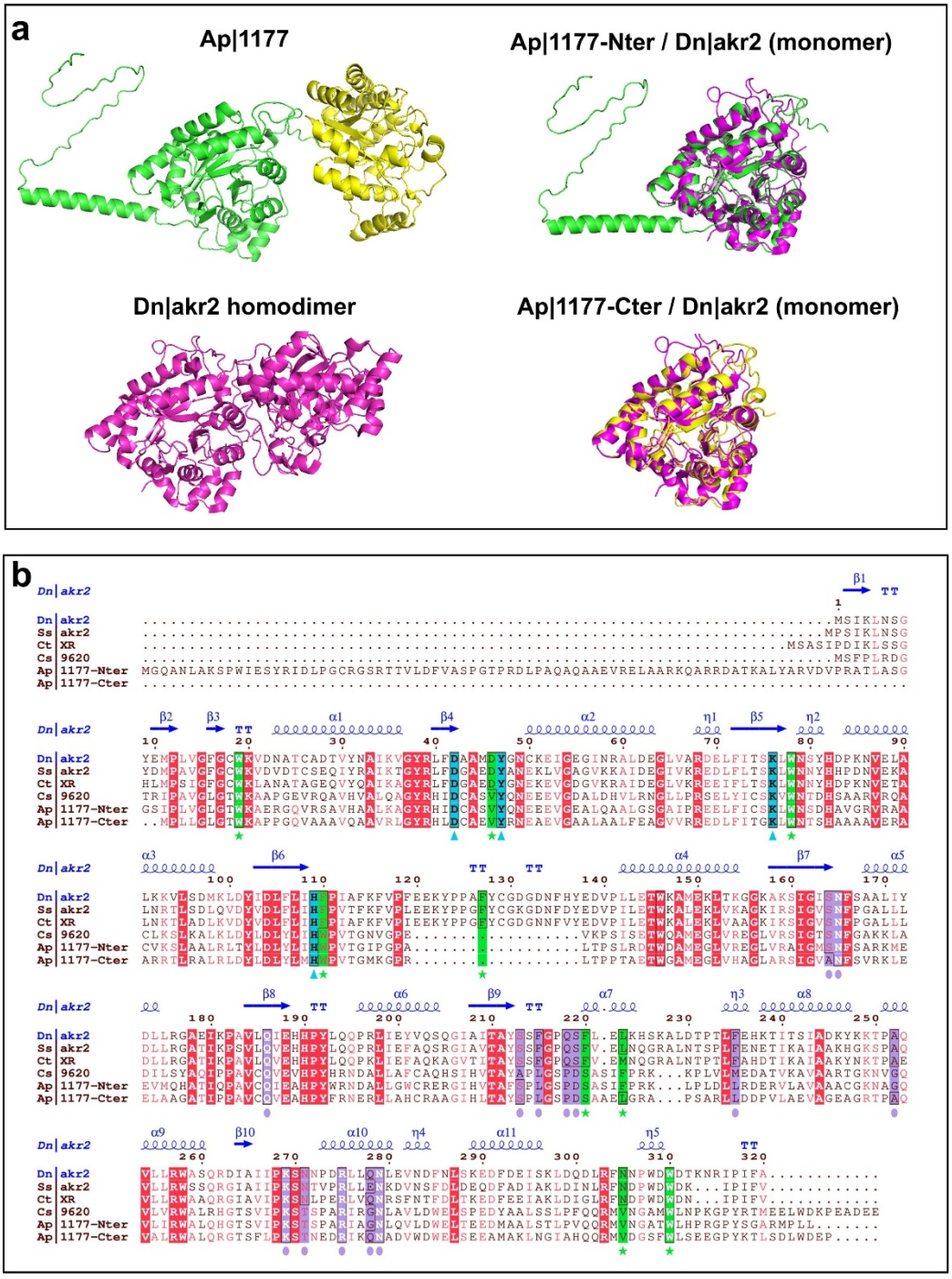

Figure 5 : (a): Predicted 3D structure of the putative A. protothecoides xylose reductase Ap|1177 compared to Dn|akr2 (in purple). The green part represents the N-terminal domain of Ap|1177 and the yellow part represents the C-terminal domain of Ap|1177. (b): Global alignment of xylose reductase of D. nepalensis (Dn|akr2), S. stipitis (Ss|akr2), C. tenuis (Ct|XR), and C. sorokiniana (Cs|9620) with the N and C-terminal domains of a putative A. protothecoides xylose reductase (Ap|1177). The amino acids MGQ at the N-terminus of Ap|1177 were added after examination of expressed sequences of the corresponding gene. Boxes with white characters in bold show amino acid residues with strict identity. Red characters show conserved function in amino acid residues among groups. Blue triangle labels show positions of the AKR family catalytic tetrad. Green star labels show positions of key amino acid residues for xylose binding. Purple circle labels show positions of key amino acid residues for NADPH-specificity. Black frames highlight strictly conserved amino acid residues across groups compared to Dn|akr2. Top secondary structures found in Dn|akr2 are marked in blue.

family (AKR2B) (Paidimuddala et al. 2018). A candidate protein, Ap|1177, was identified, displaying 20% sequence identity with Dn|akr2. However, Ap|1177 was notably longer (675 residues) compared to Dn|akr2 (320 residues). Structural modeling revealed that

Ap|1177 consists of two globular domains with similar secondary and tertiary structures, except for the first 83 residues at the N-terminal region (**Fig. 5a-b**). In addition, the N-terminal (Ap|1177-Nter) and C-terminal (Ap|1177-Cter) domains of the protein shared 56.61% sequence identity. A multiple sequence alignment with known XRs, including *Scheffersomyces stipitis* (Ss|akr2) (Son et al. 2018), and *Candida tenuis* (Ct|XR) (Petschacher and Nidetzky 2005; Kratzer et al. 2006), revealed that Ap|1177-Nter and Ap|1177-Cter shared 38.41% and 39.15% identity with Dn|akr2, respectively (**Fig. 5b, Table S2**). A putative XR from *C. sorokiniana* found by bioinformatic analysis (Cs|9620) was also included in the alignment, since cell extracts demonstrated XR activity (Zheng et al. 2014). Enzymes from the AKR2 family are typically active as homodimer in solution (Petschacher and Nidetzky 2005; Kratzer et al. 2006; Son et al. 2018). Structural prediction showed good superimposition of each domain of Ap|1177 to Dn|akr2 (**Fig. 5a**). These findings suggest that the N- and C-terminal domains of Ap|1177 function cooperatively, mimicking an active AKR2 homodimer. Consequently, each domain was analyzed individually through *in silico* approaches to further assess its potential role in xylose metabolism.

The conserved catalytic tetrad (D42, Y47, K76, H109) found in all AKR families, which is crucial for proton transfer and hydride donation in XR enzyme (Paidimuddala et al. 2018) was present in both Ap|1177-Nter and -Cter domains (**Fig. 5b, Table S2**). Among NADPH-binding residues identified in Ss|akr2 (Son et al., 2018), N165, Q186, S213, K269, and R275 were fully conserved in both Ap|1177-Nter and Ap|1177-Cter domains, while S164, A252 and Q278 residues were retained in at least one domain (**Fig. 5b**). Other NADPH related residues substituted in Ap|1177 are often identical to Cs|9620 like N271T, F215L, Q218P and S219D (**Fig. 5b, Table S2**).

Of the 10 Ss|akr2 key residues previously identified as essential in xylose-binding through site-directed mutagenesis (Son et al., 2018), five were conserved in both domains of Ap|1177, while one was retained in the C-terminal domain (**Fig. 5b**, **Table S2**). Interestingly, the remaining four positions differing in Ap|1177 matched those found in Cs|9620.

In conclusion, these findings suggest that Ap|1177 possesses most of the key residues required for XR function. Notably, Ap|1177 is structurally distinct from typical XR enzymes, as it contains two AKR2-like domains within one single protein

4. Discussion

Since *A. protothecoides* UTEX 25 was originally isolated from the sap of a wounded *Populus alba* tree rich in xylose-containing polysaccharides (Viëtor et al. 1995), the ability to uptake xylose is unsurprising. However, only a few reports describe xylose uptake by heterotrophically grown eucaryotic microalgae. Among red algae, *Galdieria sulphuraria*

was shown to assimilate xylose efficiently (Portillo et al. 2022; Perez Saura et al. 2024). In green algae, xylose uptake was demonstrated in only two uncharacterized *Desmodesmus* strains from the class of Chlorophyceae (family of the Scenedesmaceae) (Badary et al. 2024; Sartori et al. 2025), and diverse species from the class of Trebouxiophyceae (Zheng et al. 2014; Leite et al. 2015), such as *A. protothecoides* (Mu et al. 2015). Nevertheless, in the latter case, no clear evidence of net xylose assimilation was provided, as xylose was mixed with other sugars found in sugarcane bagasse hydrolysate (Mu et al. 2015). At last, a study from (Leite et al. 2015) isolated and characterized ten putative *Chlorella spp.* strains capable of xylose utilization when grown in the dark (not axenically). No report of xylitol excretion associated with xylose uptake was mentioned in these papers. As previously mentioned, only *C. sorokiniana* showed xylose uptake combined with xylitol excretion in the cultivation medium (Zheng et al. 2014).

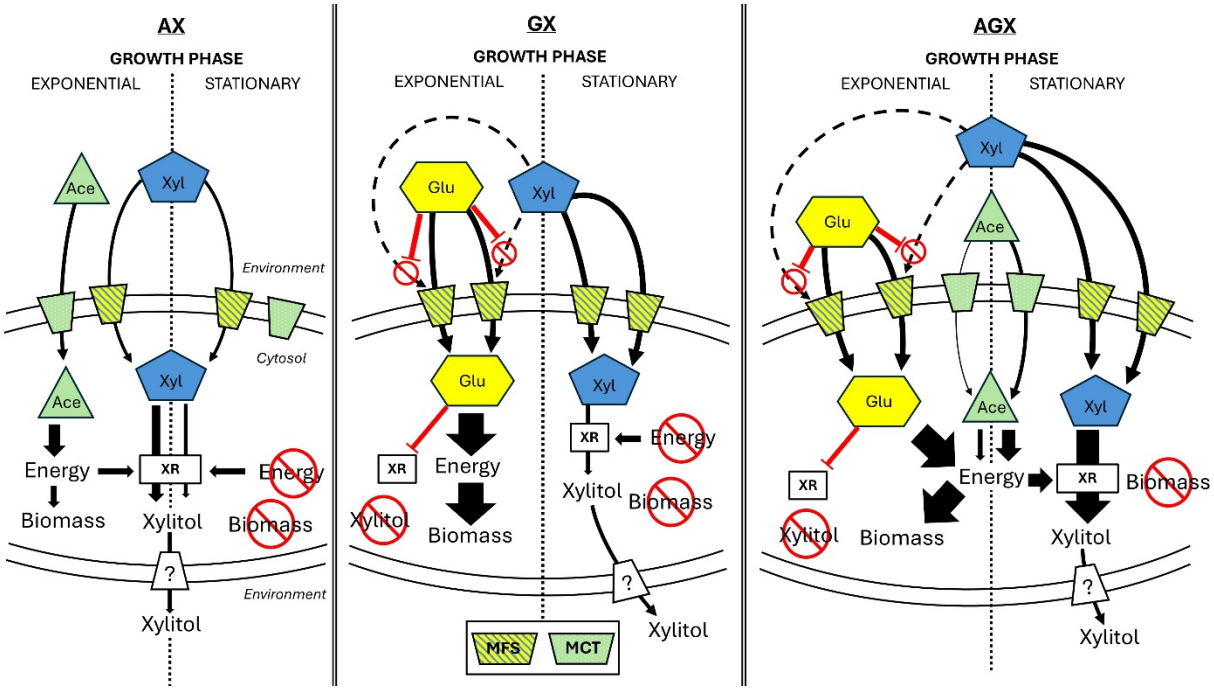

***Figure 6**: Hypothetical model of xylose conversion into xylitol of A. protothecoides grown heterotrophically in the presence of xylose and acetate (AX), of xylose and glucose (GX), or of xylose, acetate and glucose (AGX), during exponential and stationary growth phases. Substrates are represented by yellow hexagons for glucose (Glu), blue pentagons for xylose (Xyl), and green triangles for acetate (Ace). Transporters are marked trapezes colored in yellow with hashed blue line for glucose and xylose (MFS), and green with white dots for acetate (MCT). Xylose reductase (XR) is represented by a white box.*

Our data indicate that xylose metabolism in *A. protothecoides* is influenced by the presence of glucose and acetate, which modulate both xylose uptake and xylitol production efficiency (**Fig. 6**). When acetate was the sole added carbon source (AX), xylose uptake and xylitol excretion occurred gradually alongside acetate consumption. Since both xylose consumption and xylitol production rates were equally low compared to AGX, this suggests that xylose transport was limited in the absence of glucose-induced facilitation. Additionally, acetate and xylose uptakes did not appear to compete, likely

because they utilize different transport systems. Acetate is transported across the membrane via monocarboxylate transporters (MCTs) (Casal and Leão 1995; Inwongwan et al. 2019), whereas xylose is taken up by sugar transporters belonging to the Major Facilitators Superfamily (MFS) (Sun et al. 2012; Drew et al. 2021). Considering xylitol excretion, it is suggested to be mediated by an aquaglyceroporin in yeast (Wei et al. 2013). In the presence of glucose (GX), xylose uptake is initially inhibited, likely due to higher glucose affinity for shared transporters, thereby outcompeting xylose. However, once glucose was depleted, xylose uptake accelerated rapidly. Despite this, the overall conversion of xylose to xylitol remained limited, as the culture quickly entered the stationary phase, likely due to energy reallocation. This resulted in a xylitol production rate more than 2-fold lower than the xylose consumption rate. In contrast, the AGX condition revealed a synergistic effect between glucose and acetate. Here, xylose uptake was presumably enhanced following glucose depletion due to the induction of hexose transporters, similar to what was observed in GX. Meanwhile, acetate contributed to sustaine metabolic activity, allowing xylose assimilation via the glucose transporters while maintaining redox balance, as seen in AX. This combination ensured both high xylose consumption and efficient xylitol production rates. In conclusion, our findings highlight that while glucose dictates the timing of xylose metabolism, acetate plays a key role in maintaining redox balance and enzymatic activity, ultimately optimizing xylitol yield.

The fed-batch strategy shown here appears promising if the main objective is maximizing net xylitol production. While the maximal volumetric xylitol productivity observed in this study (0.57 ± 0.03 g L^{-1} d^{-1}) is low compared to xylitol-producing microorganisms reported in literature, such as *Candida tropicalis* (e.g. ~67 g L^{-1} d^{-1}), or engineered *E. coli* (~50 g L^{-1} d^{-1}) (Morais Junior et al. 2019; Yuan et al. 2019), our data provide valuable insights into xylitol production by microalgae, particularly in terms of achieving high xylose-to-xylitol yield. This strategy could begin with a high glucose concentration as a first step to obtain high cell density since *A. protothecoides* is able to grow on glucose concentrations higher than 75 $g_{glucose}L^{-1}$ (Ghidossi et al., 2017), followed by the addition of xylose and acetate once glucose is consumed. The presence of glucose will induce hexose transporters that will be used for xylose entry in the second step while acetate will bring the carbon source for xylose conversion into xylitol. The remaining biomass at the end of the xylitol excretion could be used for food since this microalga is GRAS (see introduction) and contains high percentage of fatty acids and proteins (20-30% DW) at stationary phase when cells are grown on glucose, acetate or a mix of glucose, acetate and xylose (Perez Saura et al. 2024).

XRs from yeasts are homodimeric enzymes encoded by a single gene (Petschacher and Nidetzky 2005; Kratzer et al. 2006; Son et al. 2018). The putative xylose reductase of *A. protothecoides* presents an unusual organization since the two monomers-like domains are not strictly identical and found encoded side by side in a single gene. In addition,

compared to the yeast XRs, an extension comprising an alpha helix is found at the N-terminal part. This alpha helix is probably not involved in the insertion to the membrane since no transmembrane helices are predicted by *in silico* analyses (Hallgren et al. 2022). A protein identical to Ap|1177 was found in in another strain of *A. protothecoides* (*A. protothecoides* strain 0710, Ap|4914). Amongst the genome sequences of algae found on the PhycoCosm website (Grigoriev et al., 2021), similar proteins were found for example in the green microalgae *Picichlorum soloecismus* DOE101 (Trebouxiophyceae), and *Scenedesmus obliquus* UTEX 3031 haplotype 1 (Chlorophyceae) (**Suppl. Fig. S4**), that shows slow xylose assimilation in mixotrophic conditions (Yang et al. 2014).

In summary, these findings pave the way for further optimization of sustainable xylitol bioproduction in microalgae, potentially through high cell density cultivation systems or metabolic engineering strategies to enhance transport efficiency and enzymatic activity.

1

References:

Abramson J, Adler J, Dunger J, et al (2024) Accurate structure prediction of biomolecular interactions with AlphaFold 3. Nature 630:493–500. https://doi.org/10.1038/s41586-024-07487-w

Badary A, Hidasi N, Ferrari S, Mayfield SP (2024) Isolation and characterization of microalgae strains able to grow on complex biomass hydrolysate for industrial application. Algal Research 78:103381. https://doi.org/10.1016/j.algal.2023.103381

Bueno JGR, Borelli G, Corrêa TLR, et al (2020) Novel xylose transporter Cs4130 expands the sugar uptake repertoire in recombinant *Saccharomyces cerevisia*e strains at high xylose concentrations. Biotechnol Biofuels 13:145. https://doi.org/10.1186/s13068-020-01782-0

Caporgno MP, Haberkorn I, Böcker L, Mathys A (2019) Cultivation of *Chlorella protothecoides* under different growth modes and its utilisation in oil/water emulsions. Bioresource Technology 288:121476. https://doi.org/10.1016/j.biortech.2019.121476

Carone M, Corato A, Dauvrin T, et al (2019) Heterotrophic Growth of Microalgae. In: Hallmann A, Rampelotto PH (eds) Grand Challenges in Algae Biotechnology. Springer International Publishing, Cham, pp 71–109

Casal M, Leão C (1995) Utilization of short-chain monocarboxylic acids by the yeast *Torulaspora delbrueckii*: Specificity of the transport systems and their regulation. Biochimica et Biophysica Acta (BBA) - Molecular Cell Research 1267:122–130. https://doi.org/10.1016/0167-4889(95)00067-3

Drew D, North RA, Nagarathinam K, Tanabe M (2021) Structures and General Transport Mechanisms by the Major Facilitator Superfamily (MFS). Chem Rev 121:5289–5335. https://doi.org/10.1021/acs.chemrev.0c00983

Faham S, Watanabe A, Besserer GM, et al (2008) The Crystal Structure of a Sodium Galactose Transporter Reveals Mechanistic Insights into Na^+ /Sugar Symport. Science 321:810–814. https://doi.org/10.1126/science.1160406

Fonseca C, Olofsson K, Ferreira C, et al (2011) The glucose/xylose facilitator Gxf1 from Candida intermedia expressed in a xylose-fermenting industrial strain of *Saccharomyces cerevisiae* increases xylose uptake in SSCF of wheat straw. Enzyme and Microbial Technology 48:518–525. https://doi.org/10.1016/j.enzmictec.2011.02.010

Ghidossi T, Marison I, Devery R, et al (2017) Characterization and Optimization of a Fermentation Process for the Production of High Cell Densities and Lipids Using Heterotrophic Cultivation of *Chlorella protothecoides*. Industrial Biotechnology 13:253–259. https://doi.org/10.1089/ind.2017.0007

Goold HD, Moseley JL, Lauersen KJ (2024) The synthetic future of algal genomes. Cell Genomics 4:100505. https://doi.org/10.1016/j.xgen.2024.100505

Gorman DS, Levine RP (1965) Cytochrome f and plastocyanin: their sequence in the photosynthetic electron transport chain of *Chlamydomonas reinhardi*. Proc Natl Acad Sci USA 54:1665–1669. https://doi.org/10.1073/pnas.54.6.1665

Grigoriev IV, Hayes RD, Calhoun S, et al (2021) PhycoCosm, a comparative algal genomics resource. Nucleic Acids Research 49:D1004–D1011. https://doi.org/10.1093/nar/gkaa898

Gupta R, Mthembu LD, Deenadayalu N (2022) Strain Improvement Methods for Enhanced Xylitol Production. In: de Almeida Felipe M das G, Chandel AK (eds) Current Advances in Biotechnological Production of Xylitol: Fermentative Production of Xylitol. Springer International Publishing, Cham, pp 67–80

Hallgren J, Tsirigos KD, Pedersen MD, et al (2022) DeepTMHMM predicts alpha and beta transmembrane proteins using deep neural networks. BioRxiv, https://doi.org/10.1101/2022.04.08.487609

Heredia-Arroyo T, Wei W, Hu B (2010) Oil Accumulation via Heterotrophic/Mixotrophic *Chlorella protothecoide*s. Appl Biochem Biotechnol 162:1978–1995. https://doi.org/10.1007/s12010-010-8974-4

Inwongwan S, Kruger NJ, Ratcliffe RG, O'Neill EC (2019) Euglena Central Metabolic Pathways and Their Subcellular Locations. Metabolites 9:115. https://doi.org/10.3390/metabo9060115

Kratzer R, Leitgeb S, Wilson DK, Nidetzky B (2006) Probing the substrate binding site of *Candida tenuis* xylose reductase (AKR2B5) with site-directed mutagenesis. Biochemical Journal 393:51–58. https://doi.org/10.1042/BJ20050831

Leandro MJ, Gonçalves P, Spencer-Martins I (2006) Two glucose/xylose transporter genes from the yeast *Candida intermedia* : first molecular characterization of a yeast xylose–H+ symporter. Biochemical Journal 395:543–549. https://doi.org/10.1042/BJ20051465

Leite GB, Paranjape K, Abdelaziz AEM, Hallenbeck PC (2015) Utilization of biodiesel-derived glycerol or xylose for increased growth and lipid production by indigenous microalgae. Bioresource Technology 184:123–130. https://doi.org/10.1016/j.biortech.2014.10.117

Madeira F, Madhusoodanan N, Lee J, et al (2024) The EMBL-EBI Job Dispatcher sequence analysis tools framework in 2024. Nucleic Acids Res 52:W521–W525. https://doi.org/10.1093/nar/gkae241

Miazek K, Remacle C, Richel A, Goffin D (2017) Beech wood *Fagus sylvatica* dilute-acid hydrolysate as a feedstock to support Chlorella sorokiniana biomass, fatty acid and pigment production. Bioresource Technology 230:122–131. https://doi.org/10.1016/j.biortech.2017.01.034

Morais Junior WG, Pacheco TF, Trichez D, et al (2019) Xylitol production on sugarcane biomass hydrolysate by newly identified *Candida tropicalis* JA2 strain. Yeast 36:349–361. https://doi.org/10.1002/yea.3394

Mu J, Li S, Chen D, et al (2015) Enhanced biomass and oil production from sugarcane bagasse hydrolysate (SBH) by heterotrophic oleaginous microalga *Chlorella protothecoides*. Bioresource Technology 185:99–105. https://doi.org/10.1016/j.biortech.2015.02.082

Paidimuddala B, Mohapatra SB, Gummadi SN, Manoj N (2018) Crystal structure of yeast xylose reductase in complex with a novel NADP - DTT adduct provides insights into substrate

recognition and catalysis. The FEBS Journal 285:4445–4464. https://doi.org/10.1111/febs.14667

Paulsen PA, Custódio TF, Pedersen BP (2019) Crystal structure of the plant symporter STP10 illuminates sugar uptake mechanism in monosaccharide transporter superfamily. Nat Commun 10:407. https://doi.org/10.1038/s41467-018-08176-9

Perez Saura P, Gérin S, Cardol P, Remacle C (2024) Xylose, glucose and acetate as feedstock for three microalgal species cultivated in heterotrophy. Algal Research 83:103689. https://doi.org/10.1016/j.algal.2024.103689

Petschacher B, Nidetzky B (2005) Engineering *Candida tenuis* Xylose Reductase for Improved Utilization of NADH: Antagonistic Effects of Multiple Side Chain Replacements and Performance of Site-Directed Mutants under Simulated In Vivo Conditions. Appl Environ Microbiol 71:6390–6393. https://doi.org/10.1128/AEM.71.10.6390-6393.2005

Portillo FV-L, Sierra-Ibarra E, Vera-Estrella R, et al (2022) Growth and phycocyanin production with *Galdieria sulphuraria* UTEX 2919 using xylose, glucose, and corn stover hydrolysates under heterotrophy and mixotrophy. Algal Research 65:102752. https://doi.org/10.1016/j.algal.2022.102752

Prabhu AA, Thomas DJ, Ledesma-Amaro R, et al (2020) Biovalorisation of crude glycerol and xylose into xylitol by oleaginous yeast *Yarrowia lipolytica*. Microb Cell Fact 19:121. https://doi.org/10.1186/s12934-020-01378-1

Rao J, Lv Z, Chen G, Peng F (2023) Hemicellulose: Structure, chemical modification, and application. Progress in Polymer Science 140:101675. https://doi.org/10.1016/j.progpolymsci.2023.101675

Ribeiro LE, Albuini FM, Castro AG, et al (2021) Influence of glucose on xylose metabolization by *Spathaspora passalidarum*. Fungal Genetics and Biology 157:103624. https://doi.org/10.1016/j.fgb.2021.103624

Robert X, Gouet P (2014) Deciphering key features in protein structures with the new ENDscript server. Nucleic Acids Research 42:W320–W324. https://doi.org/10.1093/nar/gku316

Runquist D, Hahn-Hägerdal B, Rådström P (2010) Comparison of heterologous xylose transporters in recombinant *Saccharomyces cerevisiae*. Biotechnol Biofuels 3:5. https://doi.org/10.1186/1754-6834-3-5

Sampaio FC, Silveira WBD, Chaves-Alves VM, et al (2003) Screening of filamentous fungi for production of xylitol from D-xylose. Braz J Microbiol 34:321–324. https://doi.org/10.1590/S1517-83822003000400007

Sartori ML, Pantoja LDA, Santos ASD (2025) Evaluation of Xylose Assimilation by a Strain of Desmodesmus sp. and the use of Sugarcane Bagasse Hydrolysate as a Carbon Source for Algal Biomass Production. Waste Biomass Valor. https://doi.org/10.1007/s12649-025-02933-w

Shi X-M, Liu H-J, Zhang X-W, Chen F (1999) Production of biomass and lutein by *Chlorella protothecoides* at various glucose concentrations in heterotrophic cultures. Process Biochemistry 34:341–347. https://doi.org/10.1016/S0032-9592(98)00101-0

Son HF, Lee S-M, Kim K-J (2018) Structural insight into D-xylose utilization by xylose reductase from *Scheffersomyces stipitis*. Sci Rep 8:17442. https://doi.org/10.1038/s41598-018-35703-x

Sun L, Zeng X, Yan C, et al (2012) Crystal structure of a bacterial homologue of glucose transporters GLUT1–4. Nature 490:361–366. https://doi.org/10.1038/nature11524

Umai D, Kayalvizhi R, Kumar V, Jacob S (2022) Xylitol: Bioproduction and Applications-A Review. Front Sustain 3:826190. https://doi.org/10.3389/frsus.2022.826190

Viëtor RJ, Renard CMGC, Goldberg R, Catesson A-M (1995) Cell-wall polysaccharides in growing poplar bark tissue. International Journal of Biological Macromolecules 17:341–344. https://doi.org/10.1016/0141-8130(96)81843-5

Wei N, Xu H, Kim SR, Jin Y-S (2013) Deletion of *FPS1* , Encoding Aquaglyceroporin Fps1p, Improves Xylose Fermentation by Engineered *Saccharomyces cerevisiae*. Appl Environ Microbiol 79:3193–3201. https://doi.org/10.1128/AEM.00490-13

Yang S, Liu G, Meng Y, et al (2014) Utilization of xylose as a carbon source for mixotrophic growth of *Scenedesmus obliquus*. Bioresource Technology 172:180–185. https://doi.org/10.1016/j.biortech.2014.08.122

Yuan X, Wang J, Lin J, et al (2019) Efficient production of xylitol by the integration of multiple copies of xylose reductase gene and the deletion of Embden–Meyerhof–Parnas pathway-associated genes to enhance NADPH regeneration in *Escherichia coli*. Journal of Industrial Microbiology and Biotechnology 46:1061–1069. https://doi.org/10.1007/s10295-019-02169-3

Zha J, Yuwen M, Qian W, Wu X (2021) Yeast-Based Biosynthesis of Natural Products From Xylose. Front Bioeng Biotechnol 9:634919. https://doi.org/10.3389/fbioe.2021.634919

Zhang Y, Fernie AR (2023) The Role of TCA Cycle Enzymes in Plants. Advanced Biology 7:2200238. https://doi.org/10.1002/adbi.202200238

Zhao Z, Xian M, Liu M, Zhao G (2020) Biochemical routes for uptake and conversion of xylose by microorganisms. Biotechnol Biofuels 13:21. https://doi.org/10.1186/s13068-020-1662-x

Zheng Y, Yu X, Li T, et al (2014) Induction of D-xylose uptake and expression of NAD(P)H-linked xylose reductase and NADP + -linked xylitol dehydrogenase in the oleaginous microalga *Chlorella sorokiniana*. Biotechnol Biofuels 7:125. https://doi.org/10.1186/s13068-014-0125-7

Table Description

Table 1: Carbon sources supplied in each cultivation condition (GX, AX, AGX, or 2x-AGX). Values are presented as the percentage (%) or the concentration of the total amount of carbon atoms represented by the substrate (mMC), or by the equivalent molar concentration considering the specific carbon source molarity (mM). A (+) symbol in 2x-AGX specifies the substrate concentration added during the cultivation process as a fed-batch strategy.

Figure Description

Figure 1 : Growth curves (a), and carbon sources concentrations of carbon sources (b-d) in the culture medium of *A. protothecoides* cells grown in heterotrophy in the presence of xylose, glucose and/or acetate. Graph (a) shows dry weight evolution (in g L-1) in the AGX (blue circles), AX (green triangles), and GX (yellow squares) conditions over time (days). Graphs (b-d) represent the evolution of glucose (dashed lines – black circles), acetate (dashed lines – grey diamonds), xylose (solid lines – black crossed-red squares), and xylitol (solid lines - green triangles) concentrations (expressed in mM of carbon atoms), over time (days), in the GX (b), AX (c), and AGX (d) conditions. Each value on the graphs is presented as the mean of three independent biological replicates. Error bars represent standard deviation of the mean (± SD).

Figure 2 : Xylose and/or xylitol consumption and production parameters calculated from *A. protothecoides* cells grown in heterotrophy in the presence of xylose and: glucose (GX, yellow bars), acetate (AX, blue bars), or both carbon sources in batch (AGX, green bars) or fed-batch (2x-AGX, white dotted green bars) cultivation strategies. Bar-chart (a) shows the maximal xylose consumption (red solid bars) and xylitol production (green hatched bars) rates, expressed in g gDW^{-1} d^{-1}. Bar-chart (b) represents the ratio of xylitol concentration at the end of the culture compared to the xylose concentration at the beginning of the culture, expressed in mM of carbon atoms. Bar-charts (c) and (d) display the global xylitol production by the end of the culture compared to the total carbon sources consumed (acetate and/or glucose) provided at the start of the culture (c, expressed in g g^{-1}), or to the maximal achieved biomass in the condition (d, expressed in g gDW^{-1}). Each value on the graphs is presented as the mean of three independent biological replicates. Error bars represent standard deviation of the mean (± SD). Distinct letters on top of the bars indicate significantly different values within the same data group, according to a Student's t-test ($p < 0.05$).

Figure 3 : Growth curves (a), and concentrations of carbon sources (a-b) in the culture medium of *A. protothecoides* cells grown in heterotrophy in the presence of xylose, glucose and acetate in the 2x-AGX condition. Graph (a) shows dry weight evolution (in g L^{-1}) in the 2x-AGX (blue circles) and glucose (dashed lines – black circles), acetate (dashed lines – grey diamonds), xylose (solid lines – black crossed-red squares), and xylitol (solid lines - green triangles) concentrations (expressed in mM of carbon atoms) over time (days). Bar-chart (b) shows the evolution of xylose consumption (red filled-bars) and xylitol production (green hatched-bars) over time (days). Each value on the graphs is presented as the mean of three independent biological replicates. Error bars represent standard deviation of the mean (± SD).

Figure 4*:* Global alignment of xylose transporters of *E. coli* (Ec|xylE), *C. intermedia* (Ci|gfx1), and *A. thaliana* (At|stp10) with two putative *A. protothecoides* xylose transporters (Ap25|2974 and Ap25|5737). Boxes with white characters in bold show amino acid residues with strict identity. Red characters show conserved function in amino acid residues among groups. Blue triangle labels show positions of key amino acid residues for xylose coordination. Green star labels show positions of key amino acid residues for sugar transporter (SP) signature. Black frames highlight strictly conserved amino acid residues across groups compared to Ec|XylE. Top secondary structures (in blue) show predicted transmembrane alpha helices in Ec|xylE. Bottom secondary structures (in orange) show predicted transmembrane alpha helices in At|stp10.

Figure 5*:* (a): Predicted 3D structure of the putative *A. protothecoides* xylose reductase Ap|1177 compared to Dn|akr2 (in purple). The green part represents the N-terminal domain of Ap|1177 and the yellow part represents the C-terminal domain of Ap|1177. (b): Global alignment of xylose reductase of *D. nepalensis* (Dn|akr2), *S. stipitis* (Ss|akr2), *C. tenuis* (Ct|XR), and *C. sorokiniana* (Cs|9620) with the N and C-terminal domains of a putative *A. protothecoides* xylose reductase (Ap|1177). The amino acids MGQ at the N-terminus of Ap|1177 were added after examination of expressed sequences of the corresponding gene. Boxes with white characters in bold show amino acid residues with strict identity. Red characters show conserved function in amino acid residues among groups. Blue triangle labels show positions of the AKR family catalytic tetrad. Green star labels show positions of key amino acid residues for xylose binding. Purple circle labels show positions of key amino acid residues for NADPH-specificity. Black frames highlight strictly conserved amino acid residues across groups compared to Dn|akr2. Top secondary structures found in Dn|akr2 are marked in blue.

Figure 6 : Hypothetical model of xylose conversion into xylitol of *A. protothecoides* grown heterotrophically in the presence of xylose and acetate (AX), of xylose and glucose (GX), or of xylose, acetate and glucose (AGX), during exponential and stationary growth phases. Substrates are represented by yellow hexagons for glucose (Glu), blue pentagons for xylose (Xyl), and green triangles for acetate (Ace). Transporters are marked trapezes colored in yellow with hashed blue line for glucose and xylose (MFS), and green with white dots for acetate (MCT). Xylose reductase (XR) is represented by a white box.

Supplementary Files

Supplementary Figure S1. *A. protothecoides* cultures in the three conditions tested (from left to right: AGX, AX, GX). The presence of the carbon sources is responsible for loss of pigmentation in heterotrophic condition.

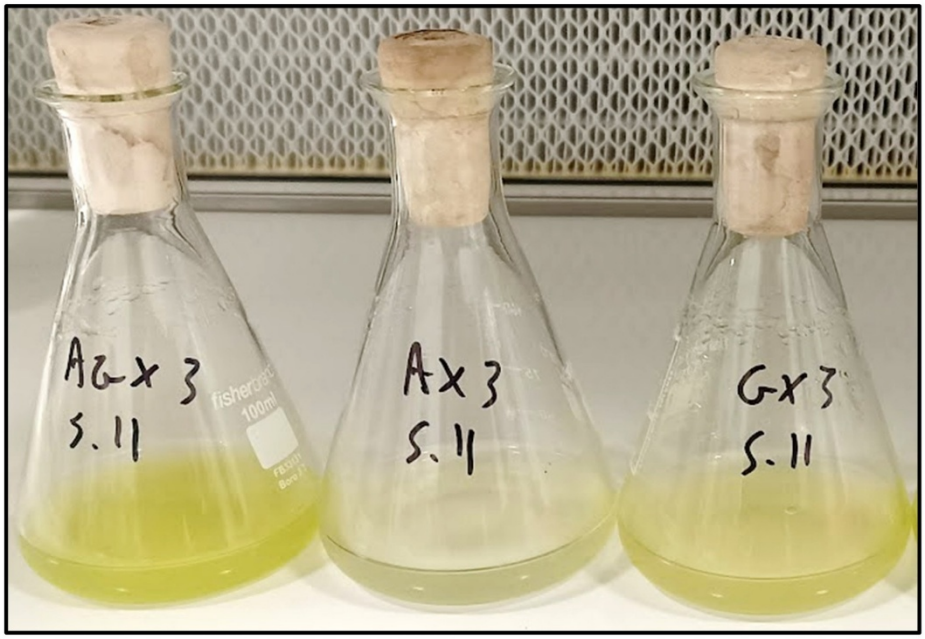

Supplementary Figure S2. HPLC chromatograms displaying the concentration of carbon sources in the cultivation medium of *A. protothecoides* under the AGX condition (acetate, glucose and xylose). (a) Chromatogram at the start of the culture. (b) Chromatogram after 90 hours of cultivation. (c) Xylitol commercial standard at 4 g L^{-1} for reference (retention time highlighted with a red line).

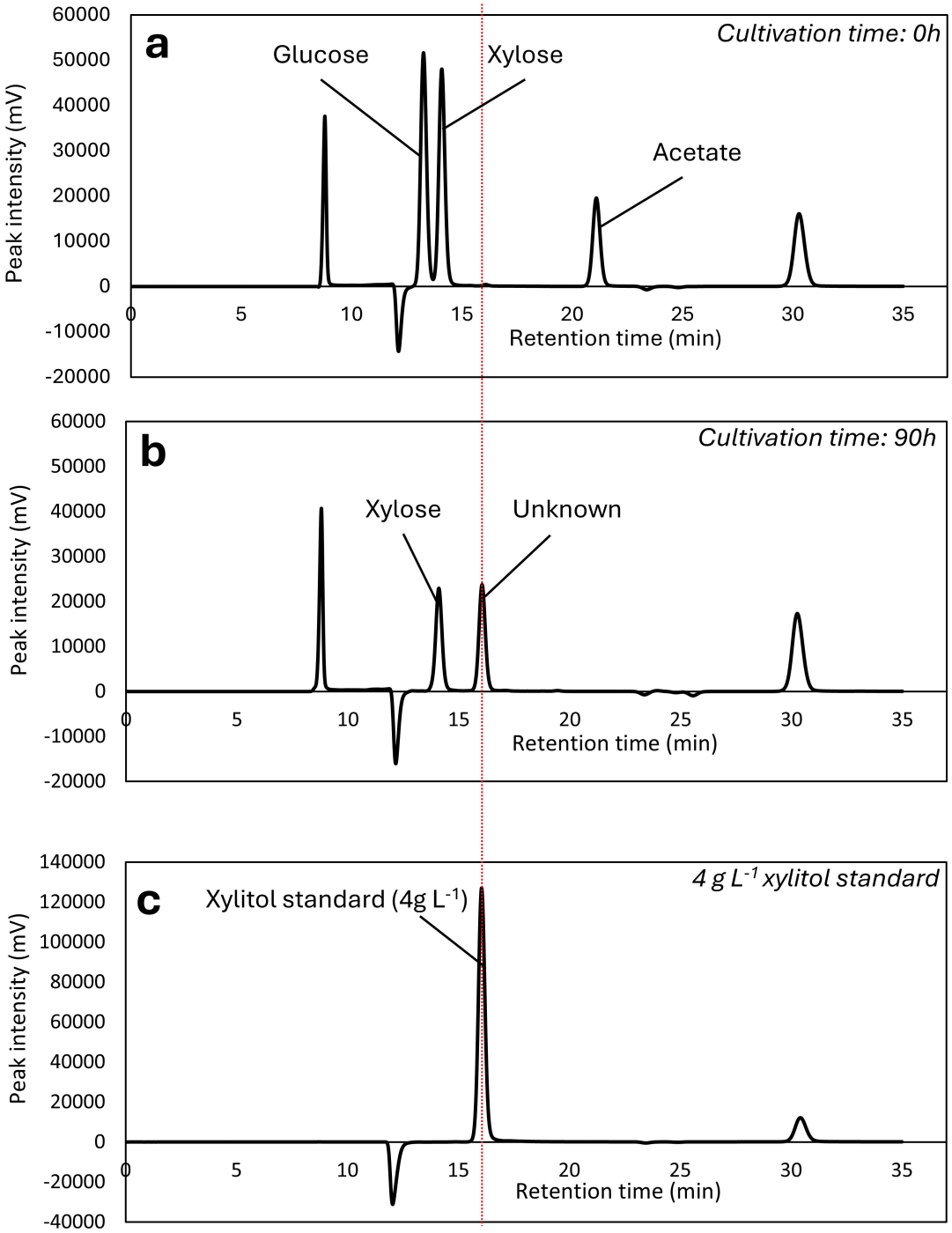

Supplementary Figure S3. Predicted 3D structure of the two putative *A. protothecoides* xylose transporters Ap|2974 (on the left) and Ap|5737 (on the right). Predicted transmembrane α helices are highlighted in blue or orange when matching to Ec|xylE or At|stp10 structure prediction, respectively. Green parts are matching with both Ec|xylE and At|stp10 structure predictions.

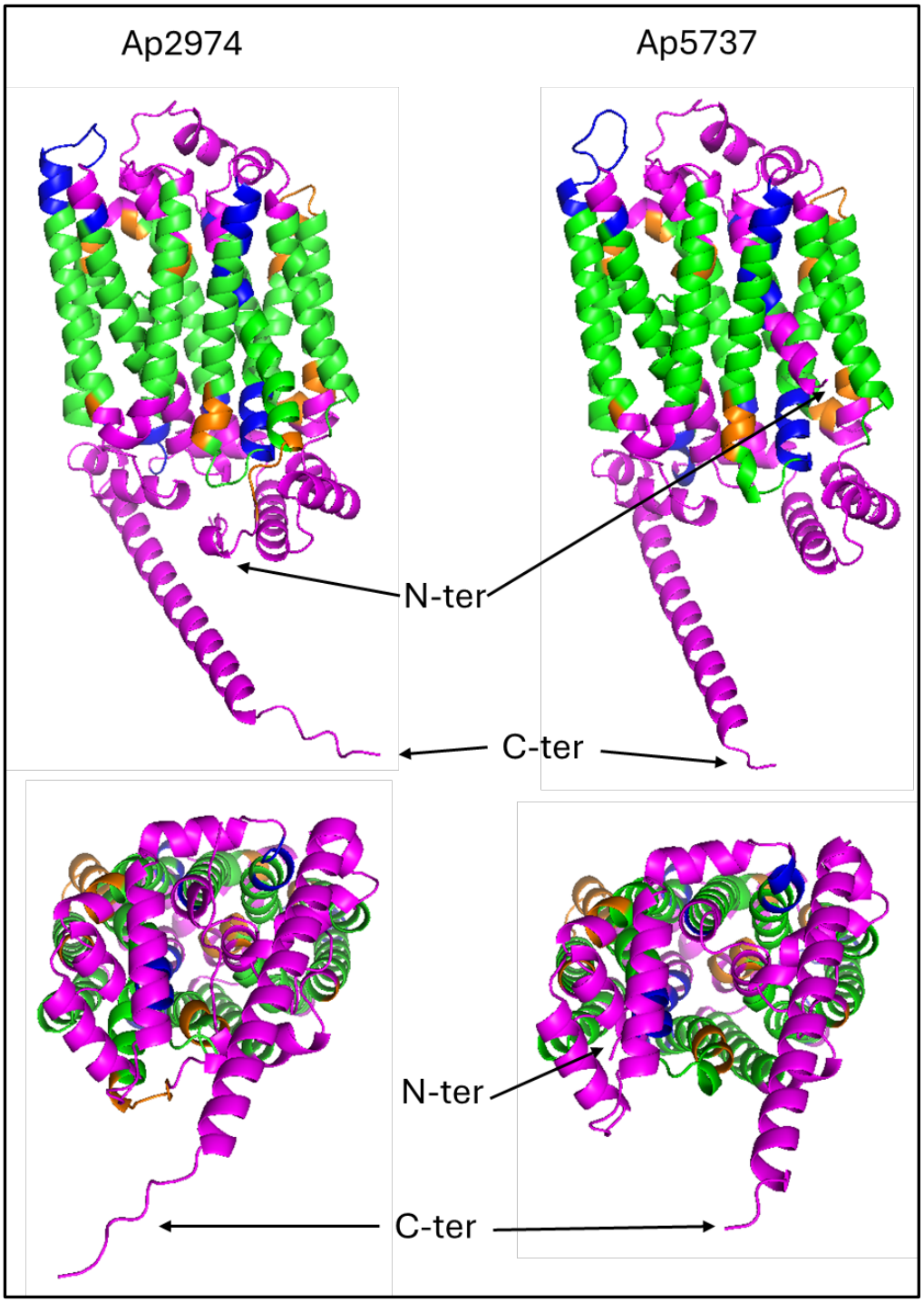

Supplementary Figure S4. Global alignment of xylose reductase of *A. protothecoides* UTEX 25 (Ap|1177), *P. soloecismus* DOE101 (Picsp_1|5253; 60.7% identity), and *S. obliquus* UTEX 3031 haplotype 1 (Sob152z_1|379; 61.9% identity). Boxes with white characters in bold show amino acid residues with strict identity. Red characters show conserved function in amino acid residues among groups. Green star labels and blue triangle labels frame the amino acid residues of the N- and C-terminal domains of Ap|1177.

Supplementary Table S1. Comparison of xylose transporters of *E. coli* (Ec|xylE), *C. intermedia* (Ci|gfx1), the putative xylose transporters of *A. protothecoides* (Ap|2974 and Ap|5737) and the *A. thaliana* hexose transporter (At|stp10) (see main text and Supplemental Fig S3 for details). Amino acids of the sugar transporter (SP) signature and xylose binding are presented.

Function	One letter code	Three letter code	Ec|xylE	Ci|gfx1	Ap|2974	Ap|5737	At|stp10
SP signature	G83	Gly	G	G	G	G	G
	E153	Glu	E	E	E	E	E
	R159	Arg	R	R	R	R	R
	S223	Ser	S	S	S	S	T
	R225	Arg	R	R	N	N	N
	G340	Gly	G	G	G	G	G
	R341	Arg	R	R	R	R	R
	E397	Glu	E	E	E	E	E
	R404	Arg	R	R	R	R	R
	E465	Glu	E	E	E	E	E
Xylose binding	F24	Phe	F	F	F	T	F
	Q168	Gln	Q	Q	Q	Q	Q
	Q288	Gln	Q	Q	Q	Q	Q
	Q289	Gln	Q	Q	Q	Q	Q
	N294	Asn	N	N	N	N	N
	Y298	Tyr	Y	Y	F	F	F
	W392	Trp	W	Y	W	W	W
	Q415	Gln	Q	N	N	N	N
	W416	Trp	W	W	F	F	M

Table S2. Comparison of xylose reductase of *Debaryomyces nepalensis* (Dn|akr2), *Scheffersomyces stipitis* (Ss|akr2), the putative XR of *C. sorokiniana* (Cs|9620) and the putative XR of *A. protothecoides* (Ap|1177-Nter and Ap|1177-Cter). Amino acids defined for the catalytic tetrad, the NADPH and xylose bindings are presented (see **Fig. 5b** and main text for details).

Function	One letter code	Three letter code	DnAKR2	SSAKR2	CtXR	Cs9620	Ap1177-Nter	Ap1177-Cter
Catalytic tetrad	D42	Asp	D	D	D	D	D	D
	Y47	Tyr	Y	Y	Y	Y	Y	Y
	K76	Lys	K	K	K	K	K	K
	H109	His	H	H	H	H	H	H
NADPH specificity	S164	S	S	S	S	S	S	A
	N165	Asn	N	N	N	N	N	N
	Q186	Gln	Q	Q	Q	Q	Q	Q
	S213	S	S	S	S	A	S	S
	F215	Phe	F	F	F	L	L	L
	Q218	Gln	Q	Q	Q	P	P	P
	S219	Ser	S	S	S	D	D	D
	F235	F	F	F	F	M	L	L
	A252	Ala	A	A	A	G	G	A
	K269	Lys	K	K	K	K	K	K
	N271	Asn	N	N	N	T	T	T
	R275	Arg	R	R	R	R	R	R
	Q278	Gln	Q	E	Q	G	G	Q
	N279	Asn	N	N	N	N	N	N
Xylose binding	W19	Trp	W	W	W	W	W	W
	D46	Asp	D	D	D	V	V	V
	W78	Trp	W	W	W	W	W	W
	H109	His	H	H	H	H	H	H
	F110	Phe	F	F	F	W	W	W
	F127	Phe	F	F	F	/	/	/
	F220	Phe	F	F	F	S	S	S
	L224	Leu	L	L	M	F	F	L
	N305	Asn	N	N	N	V	V	V
	W310	Trp	W	W	W	W	W	W

1